Generation of circularly polarized high-order harmonics by two-color coplanar field mixing

Dejan B. Milošević,* Wilhelm Becker,† and Richard Kopold
Max-Born-Institut, Max-Born-Strasse 2a, 12489 Berlin, Germany
(Received 15 December 1999; published 4 May 2000)

An efficient method is investigated for the generation of circularly polarized high-order harmonics by a bichromatic laser field whose two components with frequencies ω and 2ω are circularly polarized in the same plane, but rotate in opposite directions. The generation of intense harmonics by such a driving-field configuration was already confirmed by a previous experiment. With the help of both a semiclassical three-step model as well as a saddle-point analysis, the mechanism of harmonic generation in this case is elucidated and the plateau structure of the harmonic response and their cutoffs are established. The sensitivity of the harmonic yield and the polarization of the harmonics to imperfect circular polarization of the driving fields are investigated. Optimization of both the cutoff frequency and the harmonic efficiency with respect to the intensity ratio of the two components of the driving field is discussed. The electron trajectories responsible for the emission of particular harmonics are identified. Unlike the case of a linearly polarized driving field, they have a nonzero start velocity. By comparison with the driving-field configuration where the two components rotate in the same direction, the mechanism of the intense harmonic emission is further clarified. Depending on the (unknown) saturation intensity for the bichromatic field with counter-rotating polarizations, this scheme might be of practical interest not only because of the circular polarization of the produced harmonics, but also because of their production efficiency.

PACS number(s): 42.50.Hz, 42.65.Ky, 32.80.Qk, 32.80.Wr

I. INTRODUCTION

High-harmonic generation (HHG), besides its intrinsic interest as a highly nonlinear phenomenon of laser-atom physics (see, for example, the review article [1] and references therein), has the potential of providing a versatile source of radiation with unprecedented properties. Usually, linearly polarized driving fields have been considered which produce linearly polarized harmonics. A circularly polarized driving field does not produce circularly polarized harmonics, but rather no harmonics at all. However, circularly polarized harmonics can be generated by appropriate two-color mixing [2–6]. Such a scheme was first realized in the experiment by Eichmann *et al.* [2] who employed two circularly polarized laser fields with frequencies ω and 2ω with the electric field vectors rotating in the same plane. In the case where these two vectors rotate in the same direction, all harmonics of frequencies $n\omega$ are emitted. Their polarization is elliptic, and their intensities drop quickly with increasing harmonic order n. On the other hand, in the counter-rotating case, selection rules only allow for the emission of harmonics with frequencies $(3n\pm1)\omega$. Selection rules also require that these harmonics are circularly polarized with the sign of their helicity alternating from one harmonic to the next. In the experiment [2] no attempt was made to confirm the circular polarization of the harmonics, but the harmonic intensities were found to be high and the existence of a kind of plateau was established, which is terminated by a cutoff. Theoretical results [2,3], based on the zero-range potential model, qualitatively agree with the experimental data.

In Ref. [4] a different scheme for the production of circularly polarized harmonics is proposed. These authors suggest mixing a circularly polarized field with frequency ω and a linearly polarized field with frequency 2ω perpendicular to the former. In this case, the selection rules allow for emission of linearly polarized harmonics with frequencies $(2n+1)2\omega$ in the direction of the incident ω field and for circularly polarized harmonics with frequencies $(4n\pm1)\omega$ in the direction of the incident 2ω field [5,6]. In Ref. [4] these ideas are confirmed with calculations employing time-dependent density-functional theory. However, the intensity of the circularly polarized harmonics in this scheme is significantly lower than that of the linearly polarized harmonics of the pure one-color 2ω field. In contrast, in the counter-rotating scheme of Ref. [2] the intensity of the circularly polarized harmonics was observed to be quite high. In fact, out of various combinations of polarizations that were experimentally investigated (two parallel linear polarization, two perpendicular linear polarizations, co- and counter-rotating circular polarizations) the last mentioned setup yielded the strongest harmonic signal within a certain range of not too high harmonic frequency. Various aspects of the scheme of Ref. [4] and the scheme of the two counter-rotating circular polarizations were compared in Ref. [5]. Very recently, it has been shown [7] that the superposition of a linearly polarized laser field and a static electric field oriented at an appropriate angle to the former is also able to generate circularly polarized harmonics.

In view of the above, there is considerable practical interest in the generation of circularly polarized harmonics by two incident fields with counter-rotating circular polarizations, be it with the circular polarization of the harmonics in

*On leave from the Faculty of Science and Mathematics, Department of Physics, University of Sarajevo, Zmaja od Bosne 35, 71000 Sarajevo, Bosnia and Herzegovina.

†Also at the Center for Advanced Studies, Department of Physics and Astronomy, University of New Mexico, Albuquerque, NM 87131.

mind or just because of their high intensity. However, on the theoretical side, as pointed out in Ref. [5] and explained below, the reason of why these harmonics are produced with substantial intensity is not clear, nor is the nature of their cutoff law. One of the aims of the present paper is to explore the physical mechanism of harmonic emission in this scheme.

It is well known that the cutoff position of the harmonic spectrum, generated by a linearly polarized laser field, can be explained using the so-called three-step model [8,9]. In this classical model the atom is ionized by the laser field (first step), the freed electron starting with zero velocity moves away from the ion and back to it under the influence of the laser field (second step), in order to recombine in the third step, emitting a harmonic photon. This model yields a cutoff harmonic energy equal to the sum of the atomic ionization potential $|E_0|$ and the maximal kinetic energy acquired by the electron during its propagation in the laser field, which is $3.17U_p$ with U_p the ponderomotive energy. However, for any laser polarization other than linear, this three-step or simple-man model fails because, in this case, the ionized electron, provided it starts with zero velocity, never returns to the nucleus. A generalization of the simple-man model to the case of elliptical polarization is presented in Ref. [10]. It is based on the method of complex trajectories [11]. In the present paper we will apply the same method to the case of the two counter-rotating circularly polarized laser fields of Ref. [2]. This readily explains the mechanism of harmonic generation in this case and illustrates that actually, in contrast to initial expectation, this mechanism is quite close to that in a linearly polarized driving field. Much of the discussion is based on a semiclassical three-step model that is introduced in this paper. It is much simpler to handle than the exact method of complex trajectories without sacrificing too much information.

An outline of the paper is as follows. In Sec. II we review the strong-field approximation (SFA) theory of the HHG process and apply it to the case of a bichromatic elliptically polarized laser field. Using the saddle-point method (SPM) we show how the five-dimensional integral, that is the final result of the SFA theory, can be approximated by a single sum over the relevant complex solutions of the SPM equations, which determine the initial (ionization) time t_i and the final (recombination) time t_f. Furthermore, we will connect the obtained SPM equations with Newton's classical equation of motion for the electron in the laser field. In Sec. III we will first show that the numerical results obtained using the SFA theory reproduce previous experimental and theoretical results. We will also explore the consequences of imperfect circular polarization of the high-frequency field on the harmonic emission rate. Next, results for stronger laser fields will be shown, and the dependence of the height of the plateau and its cutoff position on the total laser intensity and its distribution over its two components will be investigated. The polarization properties of the harmonics are analyzed in Sec. IV. We will present numerical results for the harmonic ellipticity and the offset angle of the polarization ellipse for imperfect circular polarization of the high-frequency field. In Sec. V we introduce a novel semiclassical three-step model that approximates the return time by a real number. This model is employed to explain the characteristics of the plateaus and their cutoffs as they have been observed in Sec. III. We present analytical and numerical results for the cutoff law in Sec. V B. The semiclassical three-step model allows us to optimize the laser field parameters in order to increase the harmonic emission rate and the cutoff harmonic energy. Such an optimization with respect to the relative intensity of the two driving fields will be presented in Sec. V C. In Sec. V D we will discuss and plot the real-space electron orbits of the semiclassical three-step model, which are the real parts of the complex-time solutions. A more detailed explanation of the cutoff positions, as well as of the corresponding plateau structures, is presented in Sec. VI, in which we analyze the exact solutions of the saddle-point equations where all times are complex. The results are in good agreement with the numerical SFA calculations.

II. THEORY

We consider HHG by a bichromatic elliptically polarized laser field with the electric field

$$\mathbf{E}(t)=\frac{1}{2i}\left[\frac{E_1}{\sqrt{1+\varepsilon_1^2}}(\hat{\mathbf{e}}_1-i\varepsilon_1\hat{\mathbf{e}}_2)e^{i\omega t}+\frac{E_2}{\sqrt{1+\varepsilon_2^2}}(\hat{\mathbf{e}}_1-i\varepsilon_2\hat{\mathbf{e}}_2)e^{2i\omega t}\right]+\text{c.c.} \tag{1}$$

where ε_j $(-1\leqslant\varepsilon_j\leqslant 1)$ and E_j are the ellipticity and the electric field vector amplitude of the jth component of the bichromatic field, respectively, and $\hat{\mathbf{e}}_1$ and $\hat{\mathbf{e}}_2$ denote two mutually perpendicular real unit vectors. The intensity of the jth component is $I_j=\frac{1}{2}\varepsilon_0 cE_j^2$ [in the International System (SI) units; in atomic units it is $I_j=E_j^2$]. Most of the time, we will consider two corotating or two counter-rotating circularly polarized fields such that $\varepsilon_1=\varepsilon_2=1$ or $\varepsilon_1=-\varepsilon_2=1$, respectively. Examples of these two fields, for various intensity ratios I_1/I_2, are displayed in Fig. 1. They show on a quick glance that the corotating and the counter-rotating fields have a very different appearance, so it will not come as a surprise that they generate harmonics of very different character. We will return to this point on several occasions in the course of this paper. Photoionization by these fields was calculated in Ref. [12].

The vector potential corresponding to the field (1) is $\mathbf{A}(t)=-\int^t\mathbf{E}(t')dt'$. Frequently, we will use the quantity

$$\boldsymbol{\alpha}(t)=\frac{e}{m}\int^t dt'\,\mathbf{A}(t') \quad (e=|e|). \tag{2}$$

Its physical meaning is the position vector of an electron accelerated by the laser field (1) with initial conditions such that its average position is zero. The ponderomotive energy of the entire field is defined by $U_p=e^2\langle\mathbf{A}^2(t)\rangle/2m=e^2E_1^2/(4m\omega^2)+e^2E_2^2/(16m\omega^2)=U_{p1}+U_{p2}$.

We will calculate the emission rate of the nth harmonic with polarization $\hat{\mathbf{e}}_j$ with the help of the formula [13,14]

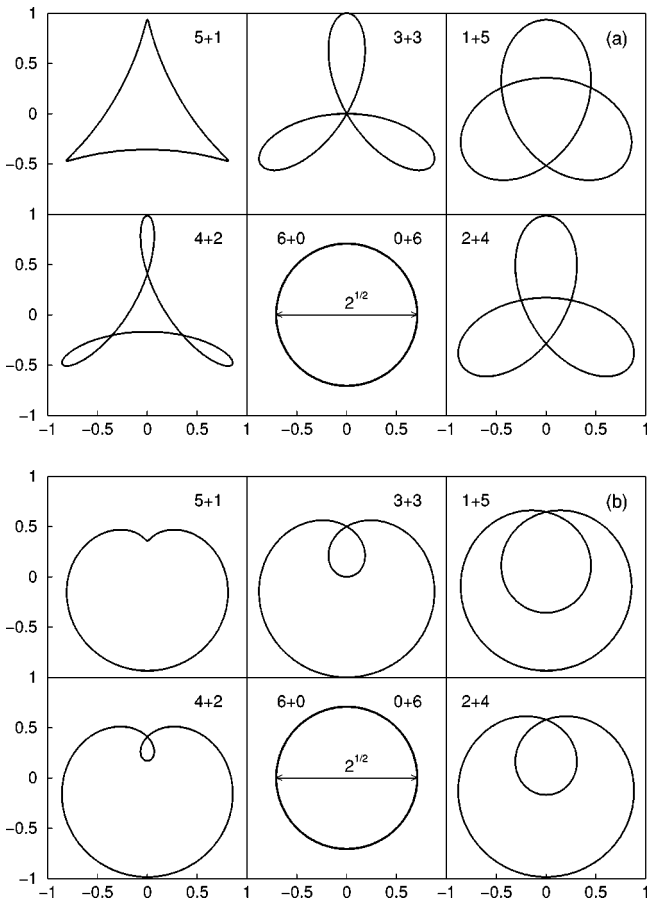

FIG. 1. The electric-field vector $\mathbf{E}(t)$, Eq. (1), of the ω-2ω counter-rotating [part (a)] and corotating [part (b)] circularly polarized laser field plotted for $0 \leqslant t \leqslant T = 2\pi/\omega$. The various panels depict the field for different combinations of the partial intensities $I_1 = i/6$ and $I_2 = j/6$ (labeled by $i+j$) such that the total intensity $I_1 + I_2 = 1$ (in arbitrary units) is constant.

$$w_n(\hat{\mathbf{e}}_j) = \frac{1}{8\pi^2 \varepsilon_0 \hbar} \left(\frac{n\omega}{c} \right)^3 |T_n(\hat{\mathbf{e}}_j)|^2, \tag{3}$$

where the T-matrix element is

$$T_n(\hat{\mathbf{e}}_j) = \int_{t_0}^{t_0+T} \frac{dt_f}{T}\, \hat{\mathbf{e}}_j^* \cdot \mathbf{d}(t_f) \exp(in\omega t_f), \tag{4}$$

with $T = 2\pi/\omega$ and arbitrary t_0. The time-dependent dipole matrix element $\mathbf{d}(t_f)$ between the initial and final laser-dressed atomic states, within the SFA [15], can be approximated by [14,11,16,17]

$$\mathbf{d}(t_f) = -\frac{i}{\hbar} \int d^3\mathbf{q} \langle \psi_0 | e\mathbf{r} | \mathbf{q} + \frac{e}{\hbar}\mathbf{A}(t_f) \rangle \times \int_{-\infty}^{t_f} dt_i \langle \mathbf{q} + \frac{e}{\hbar}\mathbf{A}(t_i) | e\mathbf{r} \cdot \mathbf{E}(t_i) | \psi_0 \rangle \times \exp\left\{ -\frac{i}{2m\hbar} \int_{t_i}^{t_f} dt [\hbar\mathbf{q} + e\mathbf{A}(t)]^2 + \frac{i}{\hbar} E_0 (t_f - t_i) \right\}, \tag{5}$$

where $|\psi_0\rangle$ and $E_0 = -|E_0|$ are the atomic ground state and its energy, respectively. The terms in the exponent in Eqs. (4) and (5) can be combined into $-iS/\hbar$. Here the quasiclassical action S consists of three terms

$$S(\mathbf{q}, t_i, t_f) = \int_{t_f}^{\infty} (E_0 + n\hbar\omega) dt + \frac{1}{2m} \int_{t_i}^{t_f} dt [\hbar\mathbf{q} + e\mathbf{A}(t)]^2 + \int_{-\infty}^{t_i} dt E_0 . \tag{6}$$

The equations (4)–(6) illuminate how the three-step model is embedded into a fully quantum-mechanical description: the atom, which is in its ground state $|\psi_0\rangle \exp(-iE_0 t/\hbar)$, tunnels into the continuum at some initial time t_i due to the interaction $e\mathbf{r} \cdot \mathbf{E}(t_i)$ with the laser field [for times less than t_i the ground state is unperturbed by the laser field, which can be seen from the last term on the right-hand side of Eq. (6)]. Afterwards, the binding potential is neglected and the ionized electron propagates in the laser field [the second term on the right-hand side of Eq. (6)]. At some final time t_f the electron returns to its starting point at the position of the ion and recombines, emitting a harmonic photon with the energy $n\hbar\omega$. The T-matrix element (4) specifies emission of such a photon with polarization $\hat{\mathbf{e}}_j$ [see the first term on the right-hand side in Eq. (6) and Eq. (4)]. The five-dimensional integral in Eqs. (4) and (5) is over all initial and final times and over all intermediate electron momenta. The total Hamiltonian has a period of T so that, in the transition from the S matrix to the T matrix in Eq. (4), the limits $(-\infty, \infty)$ of the integral over t_f are replaced by $[t_0, t_0 + T]$ following a standard procedure [13,14]. For a hydrogenlike model atom or for a Gaussian model and for a linearly polarized laser field, the integral over the intermediate electron momenta can be calculated analytically [11]. In the more general case of a bichromatic elliptically polarized laser field, this integral can be calculated by means of the method described in Ref. [16]. We will refer to these results as ''exact.''

Extending the method of complex trajectories to fields that are not linearly polarized, it was shown in Ref. [10] that the above five-dimensional integral can, to an excellent approximation, be evaluated by means of the saddle-point method. The result has the form

$$T_n(\hat{\mathbf{e}}_j) \propto \sum_s M_s \left[\det\left(\frac{\partial^2 S}{\partial q_k \partial q_l} \right) \right]^{-1/2} \exp\left(-\frac{i}{\hbar} S_s \right), \tag{7}$$

where $S_s \equiv S(\mathbf{q}_s, t_{is}, t_{fs})$ is the action (6) evaluated at the saddle points, the quantity $M_s \equiv M(\mathbf{q}_s, t_{is}, t_{fs})$ is the product of the (nonexponential) matrix elements in Eq. (5), and q_i $(i = 1, \ldots, 5)$ combines the five variables $\mathbf{q}_s \equiv (q_{1s}, q_{2s}, q_{3s})$, t_{is}, and t_{fs}. The summation in Eq. (7) is over an appropriate subset of the saddle points $(\mathbf{q}_s, t_{is}, t_{fs})$, which are the solutions of the equations

$$\frac{m}{t_f - t_i} [\boldsymbol{\alpha}(t_i) - \boldsymbol{\alpha}(t_f)] = \hbar\mathbf{q}, \tag{8}$$

$$\frac{1}{2m}[\hbar\mathbf{q}+e\mathbf{A}(t_i)]^2=E_0, \tag{9}$$

$$\frac{1}{2m}[\hbar\mathbf{q}+e\mathbf{A}(t_f)]^2=n\hbar\omega+E_0. \tag{10}$$

These equations have intuitive physical meaning. Equation (8) ensures that the electron returns to its starting point $\mathbf{r}(t_f)=\mathbf{r}(t_i)$, while Eqs. (9) and (10) express energy conservation at times t_i and t_f, respectively. The right-hand side of Eq. (9) is negative, and as a consequence the solutions $(\mathbf{q}_s, t_{is}, t_{fs})$ are complex. The quantity $\mathbf{p}=\hbar\mathbf{q}$ in Eq. (8) is the canonical momentum of the electron on its orbit for $t_i \leqslant t \leqslant t_f$, which is a constant of motion. A more detailed explanation of the connection with classical mechanics will be given below. The momentum $\mathbf{p}$ can be substituted in the remaining equations (9) and (10) so that, practically, we have to solve a system of four real equations for the variables $\mathrm{Re}\, t_i$, $\mathrm{Im}\, t_i$, $\mathrm{Re}\, t_f$, and $\mathrm{Im}\, t_f$. We will present these solutions in Sec. VI.

At the end of this section it is worthwhile mentioning that the system of equations (8)–(10) can be connected with Newton's classical equation of motion for an electron in the laser field, which is $m\ddot{\mathbf{r}}(t)=-e\mathbf{E}(t)$. The solution of this equation, with the initial conditions $\mathbf{r}(t_i)=\mathbf{r}_i$ and $\mathbf{v}(t_i)=\mathbf{v}_i$, is

$$m\mathbf{v}(t)=e[\mathbf{A}(t)-\mathbf{A}(t_i)]+m\mathbf{v}_i, \tag{11}$$

$$\mathbf{r}(t)-\mathbf{r}_i=\boldsymbol{\alpha}(t)-\boldsymbol{\alpha}(t_i)-\left[\frac{e}{m}\mathbf{A}(t_i)-\mathbf{v}_i\right](t-t_i). \tag{12}$$

The condition that the electron returns to its starting point $\mathbf{r}(t_f)=\mathbf{r}_i$ leads to $m[\boldsymbol{\alpha}(t_i)-\boldsymbol{\alpha}(t_f)]/(t_f-t_i)=m\mathbf{v}_i-e\mathbf{A}(t_i)=\mathbf{p}$, which agrees with Eq. (8). The energy conserving condition (9) demands the equality of the electron's initial kinetic energy in the laser field, which is $m\mathbf{v}_i^2/2$, to its energy E_0 in the atomic ground state. This requirement can only be satisfied for a complex velocity $\mathbf{v}_i$ such that $\mathrm{Re}\,\mathbf{v}_i\cdot\mathrm{Im}\,\mathbf{v}_i=0$ and $(\mathrm{Re}\,\mathbf{v}_i)^2-(\mathrm{Im}\,\mathbf{v}_i)^2=2E_0/m$. Similarly, for the energy conserving condition at the time t_f one has $m\mathbf{v}^2(t_f)/2=n\hbar\omega+E_0$. The electron's velocity at time t_f satisfies the conditions $\mathrm{Re}\,\mathbf{v}(t_f)\cdot\mathrm{Im}\,\mathbf{v}(t_f)=0$ and $[\mathrm{Re}\,\mathbf{v}(t_f)]^2-[\mathrm{Im}\,\mathbf{v}(t_f)]^2=2(n\hbar\omega+E_0)/m$. The complex times and velocities are alien to classical mechanics, but enforced by the electron's origin through tunneling. In Sec. V D we will show that the classical orbit can be extracted as the real part of Eq. (12).

III. NUMERICAL RESULTS FOR THE HARMONIC EMISSION RATE

In this section we will present ''exact'' results for the harmonic emission rates $\Sigma_j w_n(\hat{\mathbf{e}}_j)$, obtained by numerical integration of Eqs. (3)–(5). We will take the laser field and atomic parameters of Ref. [2]. For a hydrogenlike model atom we use the ionization potential of argon ($|E_0|=15.76$ eV), while for the zero-range potential model we use $|E_0|=11.6$ eV (see Refs. [2,3]). For the results presented in Figs. 2 and 3 we took the intensities of the two laser field components as determined in Ref. [2] in order to give an optimal description of the experimentally observed one-color spectra. These values are $I_1=1.33\times10^{14}$ W/cm^2

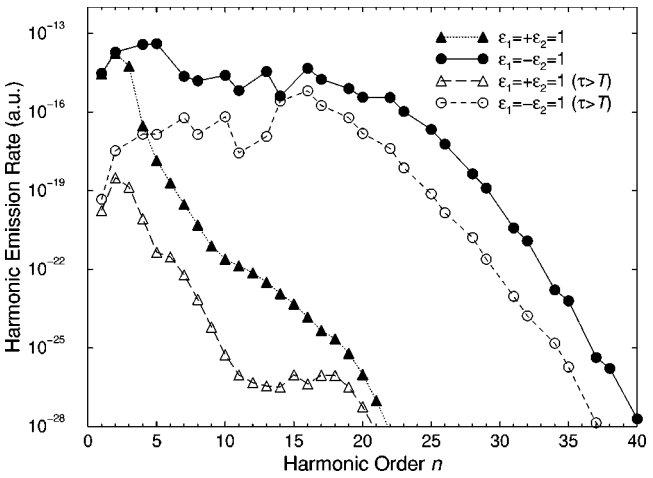

FIG. 2. Harmonic emission rates as functions of the harmonic order for the hydrogenlike model atom with the ionization potential of argon ($|E_0|=15.76$ eV). The intensities of the laser field components are $I_1=1.33\times10^{14}$ W/cm^2 and $I_2=0.58\times10^{14}$ W/cm^2. The harmonic yields for counter-rotating and corotating circularly polarized fields are represented by filled circles and triangles, respectively. Open symbols correspond to the same results obtained by neglecting those contributions to the time-dependent dipole matrix element that come from travel times $\tau=t_f-t_i$ shorter than one optical cycle T. The photon energies are $\hbar\omega_1\equiv\hbar\omega=1.6$ eV and $\hbar\omega_2=2\hbar\omega$.

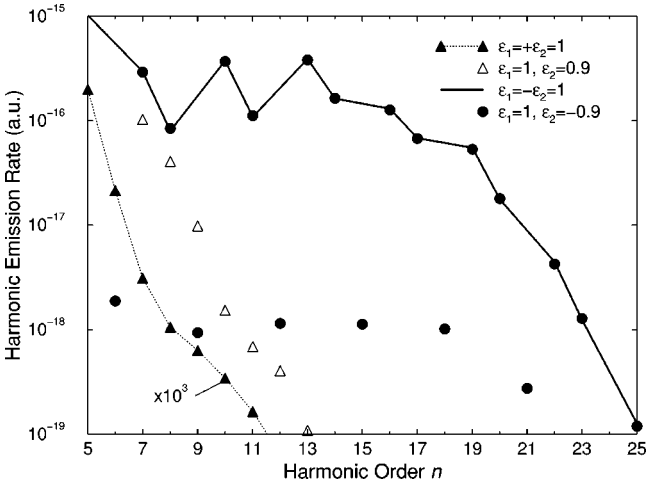

FIG. 3. Harmonic emission rates as functions of the harmonic order for the zero-range potential model with the ionization potential $|E_0|=11.6$ eV and for the same laser field intensities and frequencies as in Fig. 2. The yields for corotating fields (each multiplied by the factor 10^3) are represented by the filled (open) triangles for $\varepsilon_2=1$ ($\varepsilon_2=0.9$). The yields for the counter-rotating case are represented by a solid line for circular polarization of the second component, and by filled circles for imperfect circular polarization of the second field component, modeled by $\varepsilon_2=-0.9$.

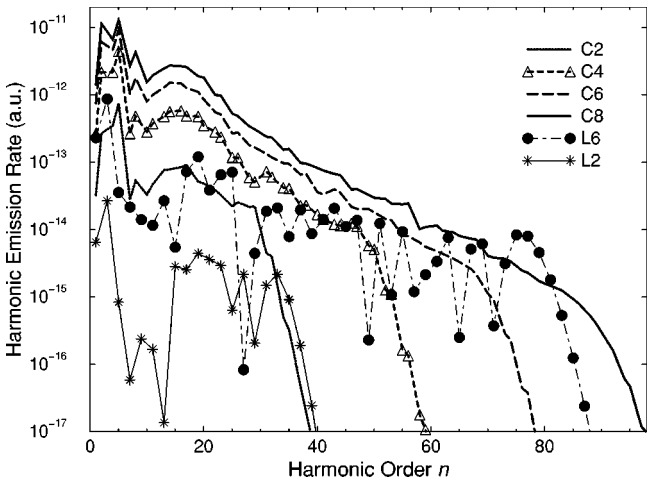

FIG. 4. Harmonic emission rates as functions of the harmonic order for the hydrogenlike model atom with ionization potential $|E_0|=15.76$ eV and equal intensities of the two counter-rotating field components such that $I_1=I_2=i\times10^{14}$ W/cm^2. The yields are labeled by Ci, where $i=2$ (dotted line), 4 (dashed line with triangles), 6 (long-dashed line), and 8 (solid line). The photon energy is $\hbar\omega=1.6$ eV. The rates for a linearly polarized monochromatic driving field with frequency ω and intensities $I=2\times10^{14}$ W/cm^2 and 6×10^{14} W/cm^2 are represented by stars and filled circles and denoted by $L2$ and $L6$, respectively.

and $I_2=0.58\times10^{14}$ W/cm^2. Results for stronger laser fields, presented in Fig. 4, correspond to equal intensities of the laser field components. The photon energies are $\hbar\omega_1\equiv\hbar\omega=1.6$ eV and $\hbar\omega_2=2\hbar\omega$.

In Fig. 2 we compare harmonic spectra obtained using the hydrogenlike model atom [11,16] for corotating ($\varepsilon_1=\varepsilon_2=1$) and for counter-rotating ($\varepsilon_1=-\varepsilon_2=1$) circularly polarized fields. One can see that in the corotating case all harmonics of frequencies $n\omega$ are emitted, but with emission rates that are much lower than those of the harmonics in the counter-rotating case. In the latter only the harmonics $(3n\pm1)\omega$ are found and they form a plateau with its cutoff around 20ω. These findings agree both with the theoretical and experimental results presented in Refs. [2,3]. In Fig. 2 we have also presented the rates obtained by excluding from the integral in Eq. (5) the contributions of travel times $\tau=t_f-t_i$ shorter than one optical cycle. The harmonic emission rates calculated in this way are, for almost all harmonics, lower by orders of magnitude than the ''exact'' results, particularly so for low-harmonic orders. This shows that the main contribution to the harmonic emission rate comes from the recombination of those electrons that return during the first optical cycle ($\tau<T$). In Sec. V D we will explicitly identify the corresponding electron trajectories.

Figure 2 immediately draws attention to the fact that the yields at a specific harmonic frequency differ by many orders of magnitude in the corotating and in the counter-rotating case. This difference largely disappears, however, if one adopts a different point of view: in the counter-rotating case, absorption of one photon with frequency 2ω and another one with frequency ω preserves angular momentum and raises the energy by 3ω. In contrast, in the corotating case, if angular momentum is to be conserved then absorption of one photon with frequency 2ω must be followed by *emission* of the photon with frequency ω, and in the combined process the energy is only raised by ω. If one assumes that the yield roughly decreases with the total number of photons emitted or absorbed, then one should compare the yield at some frequency Ω in the corotating case to the yield at 3Ω in the counter-rotating case. Indeed, these two yields are of the same order.

In Fig. 3 we display harmonic spectra for the same laser parameters as in Fig. 2, but for the zero-range potential model with $|E_0|=11.6$ eV. (In Ref. [2] this value was chosen with the reasoning that the one parameter of the zero-range potential, viz., its binding energy, should be adjusted to the energy difference between the ground state and the first excited state.) We also demonstrate the effects of imperfect circular polarization of the high-frequency field. For ellipticities $\varepsilon_1=1$ and $\varepsilon_2=-0.9$, the symmetry that prevents generation of harmonics of frequency $3n\omega$ is broken. As a consequence, these harmonics are now visible, but they are still suppressed by about two orders of magnitude. The ninth harmonic was detected in the experiment [2] and suppressed by the same amount. This suggests that the ellipticity of the 2ω field in this experiment was around 0.9. For the corotating case (triangles) the rates are again much lower. Remarkably, in this case, the harmonics for the imperfect circular polarization ($\varepsilon_2=0.9$, open triangles) have emission rates that are significantly higher, but still too low to be of any practical importance.

In Ref. [2], the saturation intensity was estimated to be 2×10^{14} W/cm^2, but for shorter pulses this intensity can be higher. Figure 4 exhibits harmonic spectra for $I_1=I_2=(2\div8)\times10^{14}$ W/cm^2. For comparison, we include the spectra for a linearly polarized monochromatic field with frequency ω having intensity $I=2\times10^{14}$ W/cm^2 (stars) and 6×10^{14} W/cm^2 (filled circles). The figure shows that the harmonic emission rates for the bichromatic counter-rotating circularly polarized fields (each of intensity I) are generally larger than those of the linearly polarized laser field (with intensity I). Furthermore, the structure of the spectra is quite different in these two cases. In contrast to the linearly polarized laser field, which generates a plateau with a rather abrupt cutoff, for the bichromatic counter-rotating circularly polarized fields two plateaus appear. The first one is higher and shorter. It is this plateau that was observed in the experiment [2]. The second plateau is longer and better described as an inclined plane. Its length is proportional to the laser intensity. Compared to linear polarization, its cutoff is less well defined.

Figure 5 compares harmonic spectra such that the total intensity of the two fields is kept constant while the ratio of the intensities of the two components varies: $I_1=i\times10^{14}$ W/cm^2 and $I_2=j\times10^{14}$ W/cm^2, where $i+j=6$. The remaining parameters are the same as in Fig. 4. The figure suggests there is an optimum value of the ratio I_2/I_1 of about 2, for which the emission rate has a maximum and the cutoff is highest. Away from this optimal ratio in either direction, but much quicker towards small values of I_2/I_1, the cutoff recedes and the yields drop. In contrast to the

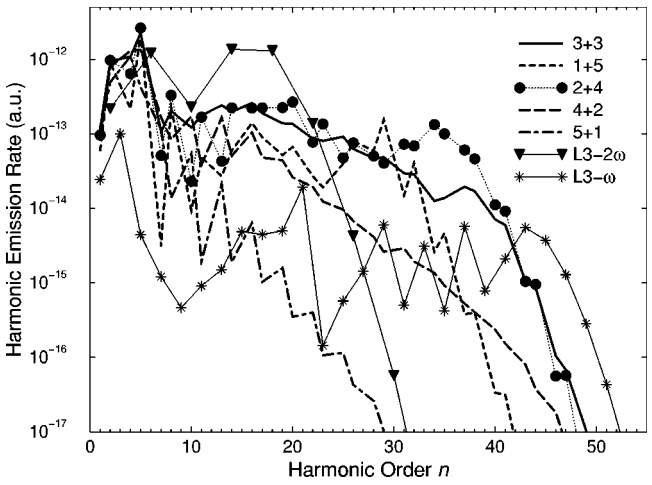

FIG. 5. Harmonic emission rates as functions of the harmonic order for various intensities of two components of the laser field such that the total intensity is constant: $I_1=i\times10^{14}$ W/cm^2 and $I_2=j\times10^{14}$ W/cm^2. In the legend the various spectra are labeled by $i+j$. Otherwise, the parameters are the same as in Fig. 4. The rates for a linearly polarized laser field with intensity $I=3\times10^{14}$ W/cm^2 are represented by stars for the frequency ω ($L3$-ω curve) and by filled triangles for the frequency 2ω ($L3$-2ω curve).

results of Fig. 4 for the lower intensities, the harmonic spectra for the cases ''2+4'' and ''1+5'' now closely resemble harmonic spectra for linear polarization. They no longer have the shape of an inclined plane.

In order to assess whether or not the scheme of the two counter-rotating circular polarizations has any advantage over the standard setup of one monochromatic linearly polarized pulse, insomuch as the harmonic efficiency is concerned, it is necessary to estimate the saturation intensities for these two scenarios. Unfortunately, there are no data available, neither experimental nor accurate theoretical, for ionization by the bichromatic counter-rotating circular polarizations. In the tunneling regime, all approximate theoretical expressions for ionization rates, such as the Ammosov, Delone, and Krainov (ADK) rate [18], are ultimately based on the paradigm of tunneling out of a short-range-potential bound state owing to an applied time-independent uniform electric field E. This rate has the form of a prefactor times the exponential

$$R\sim\exp\left(-\frac{4\sqrt{2m|E_0|^3}}{3e\hbar E}\right) \tag{13}$$

and is governed by the exponential. In order to treat a time-dependent field $\mathbf{E}(t)$ in the context of a quasistatic approximation, one may replace E by $|\mathbf{E}(t)|$ in the rate (13) and average over time. Up to a prefactor, this procedure returns the exponential (13), with E now being the peak field, as the dominant part of the rate. In those cases that are amenable to a more exact approach, such as ionization in a linearly or circularly polarized monochromatic field, this procedure has been justified. Hence, it is reasonable to assume that the exponential (13) also determines the order of magnitude of the ionization rate for the two counter-rotating circular polarizations. In view of its exponential dependence of the field, the expression (13) predicts a dramatic difference between the rates for linear and for circular polarization at the same intensity, since for the former the peak field is higher than for the latter by a factor of $\sqrt{2}$.

For our field (1) with $\varepsilon_1=\pm\varepsilon_2=1$, the peak field is $(E_1+E_2)/\sqrt{2}$ while the intensity is $I=I_1+I_2=E_1^2+E_2^2$. Let us take $E_1=E\cos\lambda$ and $E_2=E\sin\lambda$ so that the peak field is $E(\cos\lambda+\sin\lambda)/\sqrt{2}<E$. Hence, the peak field is always smaller than it would be for linear polarization, where it is just E for the same intensity $I=E^2$. However, it is not substantially smaller as long as the two intensities remain comparable. For example, for $I_2=4I_1$ we have a peak field of $0.95E$. In view of the extremely nonlinear dependence of the exponential (13) on the peak field, this may already cause substantially different ionization rates and, in consequence, saturation field strengths.

For comparison, Fig. 5 also exhibits the harmonic spectrum obtained for a linearly polarized one-color laser field. On the basis of the considerations of the previous paragraph we took for the comparison an intensity of 3×10^{14} W/cm^2, both for the frequency ω (stars) and for 2ω (solid triangles). This is half the total intensity of the two-color counter-rotating configuration. If we compare the harmonic yields of the optimal two-color configuration (''2+4'') with the one-color yields, we realize that there is a certain region of harmonics, with harmonics numbers between 25 and 40, where the two-color scheme provides the highest efficiency, by up to two orders of magnitude. For lower harmonic numbers, the linearly polarized field with frequency 2ω produces the higher yield, while for higher harmonic numbers the field with frequency ω is more efficient. If the ratio of the saturation intensities for the two-color field over the one-color field further increases, the advantage of the two-color field with regard to the one-color field becomes dramatic, otherwise it shrinks.

Figure 6 shows comparable results for helium atoms and for higher laser field intensities. The conclusions are much the same. Again, an intensity ratio of roughly 1:2 generates at the same time the most efficient harmonic output and the highest cutoff. Again, in comparison with one-color linearly polarized driving fields of either frequency, there is a window where the two-color field is most efficient. Again, the comparison was made for the one-color field having about half the total intensity of the two-color field.

IV. POLARIZATION PROPERTIES OF THE HARMONICS

According to symmetry considerations [5], in the counter-rotating case the harmonics are circularly polarized with ellipticities $\varepsilon'_{3n\pm1}=\pm1$, i.e., $\varepsilon'_4=1$, $\varepsilon'_5=-1$, $\varepsilon'_7=1$, $\varepsilon'_8=-1$, and so on. This conclusion is valid when both fields are counter-rotating exactly in the same plane and both polarizations are exactly circular. However, in any experiment invariably there will be some deviation from this ideal case. Here we consider the implications of having imperfect circular polarization for the high-frequency field such that $|\varepsilon_2|<1$. We have shown (see Fig. 3) that a small change of ε_2 has little effect on the *emission rates* of the relevant harmon-

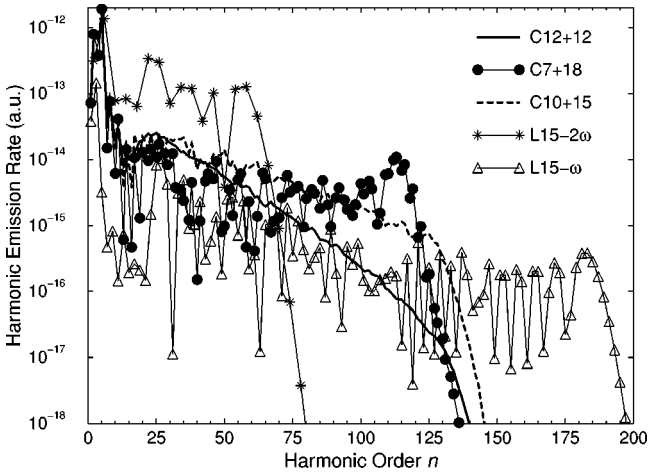

FIG. 6. Harmonic emission rates as functions of the harmonic order for helium atoms with the ionization potential $|E_0| = 24.6$ eV. The results for the bichromatic ω-2ω circularly polarized laser field with the counter-rotating components having intensities $I_1 = i \times 10^{14}$ W/cm^2 and $I_2 = j \times 10^{14}$ W/cm^2 are denoted by $Ci+j$, while the results for the monochromatic linearly polarized laser field with the intensity $I = 15 \times 10^{14}$ W/cm^2 are denoted by $L15-\omega$ and $L15-2\omega$ for the field with the frequency ω and 2ω, respectively. The laser photon energy is $\hbar\omega = 1.6$ eV.

ics. We now investigate the influence of this change on the *polarization* of the harmonics.

In order to consider the ellipticity ε_n' of the nth harmonic, we introduce the following vector, formed by the T-matrix elements (4),

$$\mathbf{T}_n = \sum_j T_n(\hat{\mathbf{e}}_j)\hat{\mathbf{e}}_j = |\mathbf{T}_n|\mathbf{e}_n', \tag{14}$$

where

$$\mathbf{e}_n' = \frac{\hat{\mathbf{e}}_{1n}' + i\varepsilon_n'\hat{\mathbf{e}}_{2n}'}{\sqrt{1+\varepsilon_n'^2}} \tag{15}$$

is a unit complex polarization vector $\mathbf{e}_n' \cdot \mathbf{e}_n'^* = 1$, and the real orthonormal unit vectors $\hat{\mathbf{e}}_{1n}'$ and $\hat{\mathbf{e}}_{2n}'$ define the nth harmonic polarization ellipse, which is rotated by an offset angle θ_n with respect to the polarization ellipse of the ω and 2ω fields (defined by $\hat{\mathbf{e}}_1$ and $\hat{\mathbf{e}}_2$). All vectors defined above are orthogonal to the wave vector $\mathbf{k} = \omega\hat{\mathbf{k}}/c$. The time-dependent nth-harmonic electric-field vector can be defined as $\mathbf{T}_n(t) = \mathrm{Re}[\mathbf{T}_n \exp(-in\omega t)]$. Generally, the ellipticity ε is connected with the circular polarization degree ζ by the formulas

$$\zeta = \frac{2\varepsilon}{1+\varepsilon^2} = i\hat{\mathbf{k}}\cdot(\mathbf{e}\times\mathbf{e}^*), \quad \varepsilon = \mathrm{sgn}(\zeta)\left(\frac{1-\sqrt{1-\zeta^2}}{1+\sqrt{1-\zeta^2}}\right)^{1/2}. \tag{16}$$

It can be shown [14,19] that the circular polarization degree ζ_n' and the offset angle θ_n of the nth harmonic can be written in terms of our T-matrix elements as

$$\zeta_n' = \frac{\mathrm{Im}\, M_n}{N_n^{(+)}}, \quad \tan 2\theta_n = \frac{\mathrm{Re}\, M_n}{N_n^{(-)}}, \tag{17}$$

where

$$N_n^{(\pm)} = |T_n(\hat{\mathbf{e}}_1)|^2 \pm |T_n(\hat{\mathbf{e}}_2)|^2, \quad M_n = 2T_n^*(\hat{\mathbf{e}}_1)T_n(\hat{\mathbf{e}}_2). \tag{18}$$

Figure 7 then presents the harmonic ellipticities ε_n' and the offset angles θ_n as functions of the harmonic order for various values of the ellipticity of the 2ω field from -0.999 to -0.85, and for two different values of the laser field intensities: (a) $I_1 = I_2 = 2 \times 10^{14}$ W/cm^2 and (b) $I_1 = I_2 = 4 \times 10^{14}$ W/cm^2. For $|\varepsilon_2|$ close to 1 the harmonic ellipticities $\varepsilon_{3n\pm1}'$ are very close to circular polarization. However, the offset angle is different from zero even for $\varepsilon_2 = -0.999$, and its value is almost independent (for the results presented) of the value of ε_2. The offset angle strongly depends on the harmonic order and on the laser field intensities, as can be seen from the bottom panels of Figs. 7(a,b). The absolute value of the harmonic ellipticity generally increases with increasing harmonic order. The influence of the imperfection of the 2ω circular polarization is larger on the ellipticity ε_{3n-1}' than on ε_{3n+1}', especially for the lower harmonics. For $\varepsilon_2 = -0.9$, the value that probably corresponds to the conditions of the experiment [2], the harmonic ellipticities ε_{3n+1}' are larger than 0.9 for $n \leqslant 13$ in Fig. 7(a), while, for example, $\varepsilon_{11}' = -0.62$.

V. A SEMICLASSICAL THREE-STEP MODEL

A. The model

The three-step model was originally formulated for HHG in a linearly polarized laser field [8,9]. In the simplest (simple-man) version of this model one supposes that the electron appears in the continuum with zero initial velocity $\mathbf{v}_i = \mathbf{0}$ at the position of its parent ion. Its subsequent classical motion in the laser field is then restricted to one dimension, viz., the direction of the laser field. The binding energy E_0 never enters this model. (We will speak of a ''simple-man model'' whenever the electron is ''put by hand'' into the continuum, i.e., whenever its binding energy is ignored.) In the case of an elliptically polarized laser field, if $\mathbf{v}_i = \mathbf{0}$ as for linear polarization, the electron never returns to its starting point and this model is no longer applicable.

We will now formulate a semiclassical three-step model that allows for both a nonzero initial velocity and a nonzero binding energy. It is because of the latter that we call it semiclassical, since invariably it will involve tunneling. Let us consider the saddle-point equations (8)–(10). As a consequence of Eq. (9), since the binding energy E_0 is negative, both the canonical momentum $\hbar\mathbf{q}$ and the start time t_i have to be complex (it is easy to convince oneself that just one or the other being complex will not solve the equations). The return time t_f then comes out complex as well. We will discuss these exact solutions of the saddle-point equations below in Sec. VI. Here we will resort to an approximation: we anticipate from Sec. VI and from earlier work [10,20] that, in

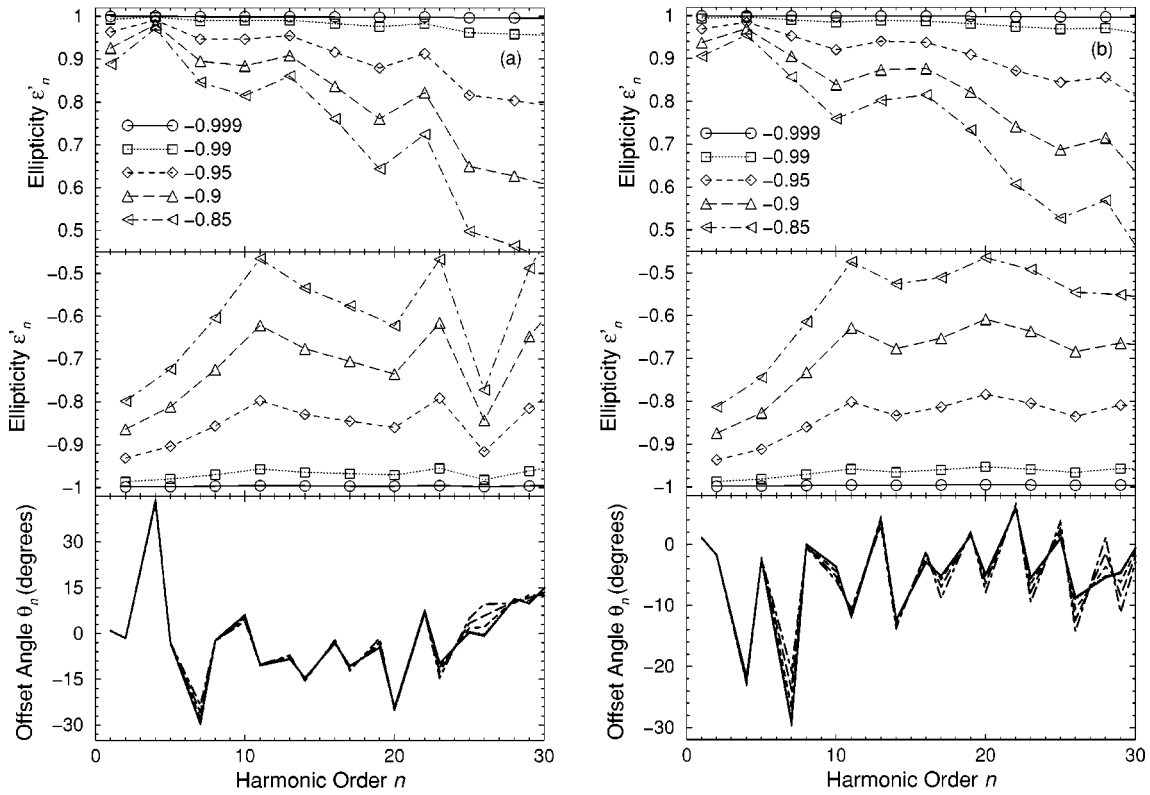

FIG. 7. Harmonic ellipticities ε_n' and offset angles θ_n as functions of the harmonic order for various values of the ellipticity of the high-frequency field: $\varepsilon_2=-0.999$ (solid curve), -0.99 (dotted curve), -0.95 (dashed curve), -0.9 (long-dashed curve), and -0.85 (dot-dashed curve), and for two different values of the laser field intensities: (a) $I_1=I_2=2\times10^{14}$ W/cm^2 and (b) $I_1=I_2=4\times10^{14}$ W/cm^2. The other parameters are the same as in Fig. 4.

marked contrast to the start time, the imaginary part of the return time is very small. Hence we will assume that the return time t_f is real.

Eliminating, first, the canonical momentum $\mathbf{q}$ with the help of Eq. (8) and, second, the start time in favor of the travel time $\tau=t_f-t_i$, we rewrite Eq. (9) as

$$\frac{1}{2m}\left\{\frac{m}{\tau}[\boldsymbol{\alpha}(t_f-\tau)-\boldsymbol{\alpha}(t_f)]+e\mathbf{A}(t_f-\tau)\right\}^2=E_0. \quad (19)$$

We will solve this equation for the travel time τ for a fixed final time t_f. The travel time τ will, of course, be complex. For each $t_f\in[t_0,t_0+T]$ there is an infinite number of solutions τ_j $(j=1,2,\ldots)$. It turns out that the set of all these solutions, $\{\tau_j(t_f),t_f\in[t_0,t_0+T],j=1,2,\ldots\}$, forms a single continuous curve in the complex τ plane such that $\mathrm{Im}\,\tau$ is a single-valued function of $\mathrm{Re}\,\tau$ [21]. Using these solutions one can both estimate the probability of harmonic emission and calculate the energy of the emitted harmonics. According to Eq. (5), the contribution from the travel time τ_j to the time-dependent dipole $\mathbf{d}(t_f)\propto\Sigma_j\mathbf{d}(t_f,\tau_j)$ is

$$|\mathbf{d}(t_f,\tau_j)|\propto\frac{\exp[\mathrm{Im}\,S(\mathbf{q},t_f-\tau_j,t_f)/\hbar]}{|\tau_j|^{3/2}}, \quad (20)$$

where the term in the exponent is the imaginary part of the quasiclassical action (6), while the factor $|\tau_j|^{3/2}$ comes from the integration over the intermediate electron momenta and reflects wave-packet spreading. Below, we will occasionally refer to $\mathbf{d}(t_f,\tau_j)$ as the partial time-dependent dipole. On the other hand, according to Eq. (10), the emitted harmonic energy $n\hbar\omega$ is the sum of the ionization potential $|E_0|$ and the electron's kinetic energy $m\mathbf{v}^2(t_f)/2$ at the moment t_f of recombination. The electron's velocity in the laser field, $\mathbf{v}(t_f)=[\mathbf{p}(t_f-\tau,t_f)+e\mathbf{A}(t_f)]/m$ is complex because τ is complex. Equation (10) now yields a complex harmonic energy since, in general, $\mathrm{Re}\,\mathbf{v}(t_f)\cdot\mathrm{Im}\,\mathbf{v}(t_f)\neq0$. This is a consequence of our assumption above of a real return time t_f. As mentioned above, the imaginary part of t_f is small and so is $\mathrm{Im}\,\mathbf{v}(t_f)$. Therefore, we will ignore the imaginary part of Eq. (10). We then have

$$n\hbar\omega=|E_0|+\frac{m}{2}\{[\mathrm{Re}\,\mathbf{v}(t_f)]^2-[\mathrm{Im}\,\mathbf{v}(t_f)]^2\},$$

$$m\mathbf{v}(t_f)=\frac{m}{\tau}[\boldsymbol{\alpha}(t_f-\tau)-\boldsymbol{\alpha}(t_f)]+e\mathbf{A}(t_f). \quad (21)$$

Let us consider the solutions for the complex time τ for the bichromatic counter-rotating circularly polarized laser field whose harmonic emission rates are given by the curve C4 in Fig. 4. In the lower panel of Fig. 8 we plot, by a solid line, the quantity $-\mathrm{Im}\,\tau$ as a function of $\mathrm{Re}\,\tau$ for $\mathrm{Re}\,\tau\in[0,2T]$. In addition to these complex solutions for τ, with

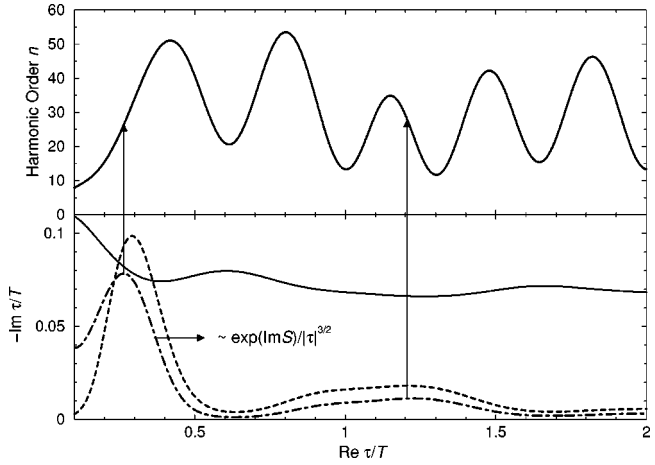

FIG. 8. Semiclassical three-step model analysis of HHG in two counter-rotating circularly polarized laser fields with photon energies $\hbar\omega=1.6$ eV and $2\hbar\omega$, and with the intensities $I_1=I_2=4\times10^{14}$ W/cm^2. The ionization potential is $|E_0|=15.76$ eV. Lower panel: Imaginary part of the complex travel time τ (solid line) and the partial time-dependent dipole $\mathbf{d}(t_f,\tau_j)$ (dot-dashed line) as functions of the real part of the travel time τ. Both Re τ and Im τ are expressed in optical cycles $T=2\pi/\omega$ (note that Im τ is negative). The exact partial time-dependent dipole (20) and its approximation (22) are represented by the dot-dashed and the dashed line, respectively, and expressed in a.u./500. Upper panel: Harmonic order n, obtained by introducing the solutions for τ into Eq. (21), as a function of the real part of τ/T. The two maxima of the estimated partial time-dependent dipole are identified by vertical arrows and connected to the curve $n=n(\mathrm{Re}\,\tau/T)$ in the upper panel.

negative values of Im τ, there are also complex conjugate solutions τ^* with positive Im τ. These are unphysical and must be discarded as they lead to an exponentially increasing emission probability. We also show in the lower panel of Fig. 8, as a dot-dashed line, the partial time-dependent dipole, obtained according to Eq. (20). Clearly, there are two regions of Re τ for which this quantity has a maximum. Presumably, these will dominate the harmonic response. The upper panel of Fig. 8 displays the harmonic energy calculated from Eq. (21) as a function of Re τ. The maxima agree with the upper cutoff in Fig. 4 around $n=50$.

The lower panel of Fig. 8 also displays, as a dashed line, an approximation to the partial emission rate (20) that is obtained using the following expansion of Im S in powers of Im τ,

$$\mathrm{Im}\,S(\mathbf{q},t_f-\tau,t_f)=-\frac{e}{3}\frac{\partial}{\partial t_{iR}}[\mathbf{E}(t_{iR})\cdot\mathbf{v}_{iR}](\mathrm{Im}\,\tau)^3+O[(\mathrm{Im}\,\tau)^5], \tag{22}$$

where $t_{iR}\equiv t_f-\mathrm{Re}\,\tau$, and the real part of the initial velocity is $\mathbf{v}_{iR}=[\boldsymbol{\alpha}(t_{iR})-\boldsymbol{\alpha}(t_f)]/\mathrm{Re}\,\tau+e\mathbf{A}(t_{iR})/m$. One can see that this approximation agrees reasonably well with the exact expression (20).

In conclusion, this semiclassical three-step model contains most of the relevant information about the HHG process. The crucial quantities are the complex travel time. These are found as solutions of the energy conserving condition at the moment of ionization. They are complex because the electron is born in a tunneling process. The imaginary part of the travel time determines the probability of the process, while the real part is related to the harmonic energy. The latter can be found using Newton's classical equation of motion for the electron in the laser field. A vital feature of the model is that the electron starts on its orbit with nonzero complex velocity whose value is determined by the condition that it return to the origin. Finally, we mention that repeating the calculations of Fig. 8 with a binding energy of zero only insignificantly changes the results. In the nomenclature that we suggested above, this would be referred to as a simpleman model.

B. Cutoff law

In Sec. V A we have shown that the main contribution to the harmonic emission rate comes from electrons with travel times such that Re $\tau<T/2$. [In Sec. VI we will show that this contribution corresponds to one particular complex trajectory, denoted by *2* in Figs. 13 and 14(a).] In this region of Re τ, the harmonic order has one maximum (see the upper part of Fig. 8) which determines the cutoff of the harmonic spectrum. This cutoff can be found as the first maximum of the function $n\hbar\omega(\tau)$, Eq. (21). For equal intensities of the laser field components $I_1=I_2$, we obtain the following cutoff law:

$$n_{\max}\hbar\omega=\frac{1}{\sqrt{2}}\,3.17U_p+1.2|E_0|. \tag{23}$$

This should be compared to the well-known cutoff law for a linearly polarized laser field: $n_{\max}\hbar\omega=3.17U_p+1.3\,|E_0|$ (see Refs. [8,11]). It agrees with the numerical results presented in Fig. 4.

For the case of different intensities of the laser field components $I_1\neq I_2$, we determine the maximum of the electron's kinetic energy $E_{\mathrm{kin,max}}$ as a function of the ratio of the intensity of the second laser field component and the total intensity $R=I_2/(I_1+I_2)$. For $E_0=0$, this is equal to the maximum of the harmonic photon energy. In Fig. 9 we plot, by a solid line, $E_{\mathrm{kin,max}}$ divided by the ponderomotive energy $U_p(R)$. In order to specify the absolute value of $E_{\mathrm{kin,max}}$ as a function of R we also present, with a dashed line, $E_{\mathrm{kin,max}}$ divided by the ponderomotive energy calculated at $I_1=I_2$. The ratio of these two ponderomotive energies is $U_p(R)/U_p(R=0.5)=2(4-3R)/5$. We exclude $R<0.05$ and $R>0.95$ because in these regions the polarization of the laser field is close to circular and the harmonic emission rate is negligible. From Fig. 9 one can see that $E_{\mathrm{kin,max}}/U_p(R)$ (solid line) increases with increasing R up to a maximum value of 2.54 at $R=0.84$. On the other hand, $E_{\mathrm{kin,max}}/U_p(R=0.5)$ (dashed line) decreases monotonically with increasing R. All of this agrees with the numerical results presented in Fig. 5.

C. Optimization of the harmonic emission rate

Figure 8 shows that the functions $\exp(\mathrm{Im}\,S/\hbar)/|\tau|^{3/2}$ and $n(\mathrm{Re}\,\tau/T)$ do not assume their maxima at the same positions.

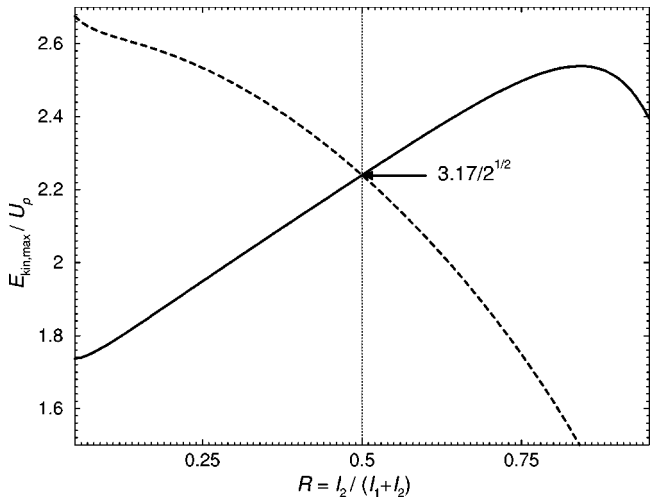

FIG. 9. The maximal kinetic energy of the electron according to the semiclassical three-step model as a function of the ratio of the intensity of the second laser field component over the total intensity $R=I_2/(I_1+I_2)$. Solid line: $E_{\mathrm{kin,max}}$ divided by the ponderomotive energy $U_p(R)$. Dashed line: $E_{\mathrm{kin,max}}$ divided by the ponderomotive energy $U_p(R=0.5)$ for equal intensities ($I_1=I_2$). The cutoff law for $I_1=I_2$, $E_{\mathrm{kin,max}}=3.17U_p/\sqrt{2}$, is emphasized in the figure.

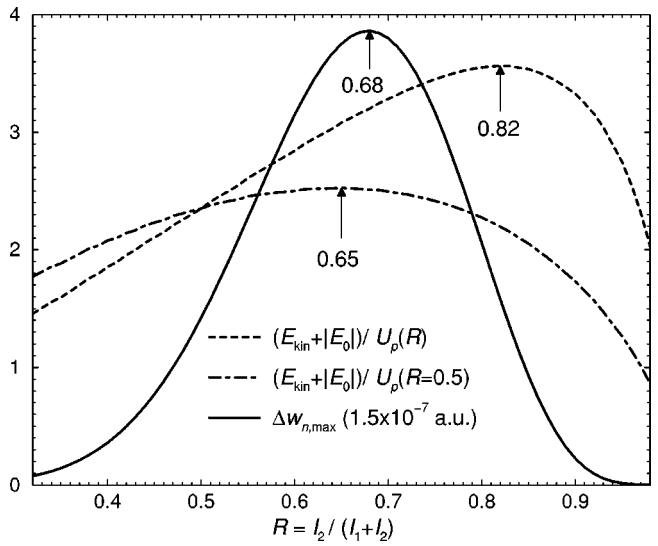

FIG. 10. Maximal partial emission rate $dw_{n,\mathrm{max}}$ (solid line) and the corresponding harmonic photon energy $n\hbar\omega=E_{\mathrm{kin}}+|E_0|$ as functions of the ratio $R=I_2/(I_1+I_2)$. The dashed (dot-dashed) line shows the harmonic photon energy divided by the ponderomotive energy $U_p(R)$ [constant ponderomotive energy $U_p(R=0.5)$]. The results are obtained from the semiclassical three-step model. The laser field and atomic parameters are the same as in Fig. 8, except that the intensities of the laser field components vary such that the sum of the intensities is constant and equals $I_1+I_2=8\times10^{14}$ W/cm^2.

In Sec. V B we have explored the cutoff harmonic order n as a function of the ratio R. It is of comparable interest to maximize the emission rate with respect to both the order n and the ratio R. Hence, in this subsection we analyze the partial emission rate $\Delta w_n(\tau)\equiv\exp(2\,\mathrm{Im}\,S/\hbar)|n/\tau|^3$. This rate can easily be obtained within our semiclassical three-step model [cf. Eq. (20)]. Figure 10 displays, as a solid line, the function $\Delta w_{n,\mathrm{max}}\equiv\max_\tau\Delta w_n(\tau)$ as a function of the normalized intensity ratio $R=I_2/(I_1+I_2)$, for $I_1+I_2=8\times10^{14}$ W/cm^2, and the other parameters as in Fig. 8. It is interesting to observe that $\Delta w_{n,\mathrm{max}}(R)$ does not reach its maximum for $I_1=I_2$, but for $I_2>I_1$. Hence, in order to attain the highest emission rate one has to employ a disproportionately large intensity of the high-frequency component. This is in agreement with the numerical results presented in Fig. 5. The optimal value of the parameter R, in the present case, is $R=0.68$, which means $I_2\approx2I_1$. The harmonic photon energy $n\hbar\omega=E_{\mathrm{kin}}+|E_0|$ that corresponds to the value of τ for which $\Delta w_n(\tau)$ has its maximum is plotted again in two different ways: scaled to the ponderomotive potential $U_p(R)$ (dashed line) and to the ponderomotive potential for equal intensities of the laser field components (dot-dashed line). In the former case, the maximum of the rate and the maximal harmonic order roughly coincide.

D. Real-space electronic trajectories

In the preceding subsections we have shown that the behavior of the harmonic emission rates can be adequately discussed in terms of electronic trajectories that have a real return time, but a complex travel time. If so, is it possible to assign physical meaning to the associated complex trajectories? Here we will make the case that the answer is affirmative.

According to Fig. 8, for a fixed n we concentrate on a particular solution τ_n which, in turn, implies an associated value of t_f. The corresponding trajectory $\mathbf{r}_n(t')$, $t_f-\mathrm{Re}\,\tau\leqslant t'\leqslant t_f$, is then obtained as the solution of the classical equation of motion [see Eq. (12)]

$$\mathbf{r}_n(t')\equiv\mathrm{Re}[\mathbf{r}(t')-\mathbf{r}(t_f-\tau)]$$
$$=\frac{\hbar}{m}(t'-t_f)\,\mathrm{Re}\,\mathbf{q}(t_f-\tau,t_f)+\boldsymbol{\alpha}(t')-\boldsymbol{\alpha}(t_f). \quad (24)$$

Similarly, for the real electron velocity along this trajectory we obtain

$$\mathbf{v}_n(t')\equiv\frac{e}{m}\mathbf{A}(t')+\frac{\hbar}{m}\,\mathrm{Re}\,\mathbf{q}(t_f-\tau,t_f). \quad (25)$$

In the preceding two equations, we have explicitly written the canonical momentum $\mathbf{q}$ as a function of its two variables $t_i=t_f-\tau$ and t_f. Notice that $\mathbf{r}_n(t_f)=0$, since we assumed t_f as real, while $\mathbf{r}(t_f-\mathrm{Re}\,\tau)\neq0$ since $t_f-\mathrm{Re}\,\tau\neq t_i$. The start time t_i is complex, after all.

In Figs. 11 and 12 we present such real-space trajectories for the same example that we have considered in Sec. V A. Figure 11 depicts the four trajectories that correspond to the first four maxima of the harmonic order as a function of the real part of τ as shown in the upper part of Fig. 8. Each curve is labeled with the corresponding values of n. The corresponding values of $\mathrm{Re}\,\tau/T$ are given in the caption of Fig. 11. As mentioned above, the curves do not start at the origin, but at some distance of about 4 a.u. away from it. In a tun-

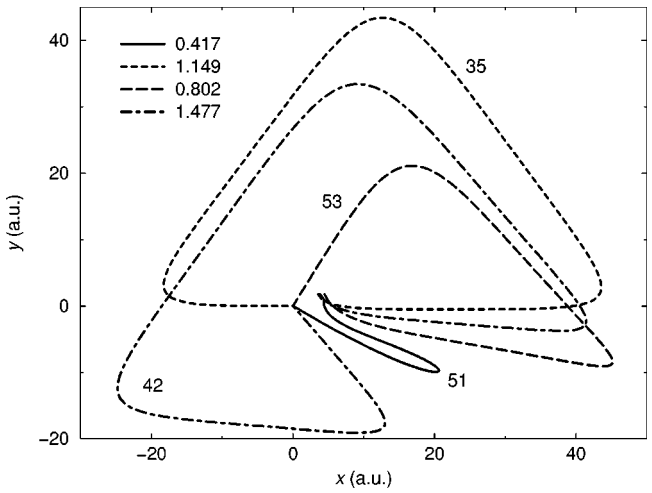

FIG. 11. Electron trajectories for the same laser field and atomic parameters as in Fig. 8, obtained from the semiclassical three-step model. Four trajectories are presented that correspond to the first four maxima of the harmonic order n as a function of the Re τ as depicted in the upper panel of Fig. 8. Each trajectory is labeled by the corresponding values of n; the respective values of Re τ/T are identified in the upper left corner.

neling picture, this would be called the ''exit of the tunnel.'' In contrast, they terminate exactly at the origin. The trajectory in Fig. 11 with the shortest travel time, labeled by $n=51$, corresponds to the first maximum of the function $n \equiv n(\mathrm{Re}\,\tau)$ in Fig. 8. This trajectory starts at the point (4.3,0.8); it first moves in the negative y direction and then slowly turns until it travels by an angle of 57.2° with respect to the negative y axis. After its maximal excursion at the point $(20.6,-9.7)$, the electron on this trajectory turns back and moves almost opposite to its former direction. Finally, it terminates exactly at the origin with the kinetic energy that allows for the emission of the harmonic $n=51$. The other orbits are longer and more complicated. They all have a triangular shape that reflects the threefold symmetry of the $\omega-2\omega$ counter-rotating circularly polarized field case [cf. Figs. 12(c) and 1]. We will show in Sec. VI that the most relevant of these trajectories is the one that corresponds to the third maximum of n in Fig. 8, labeled by $n=35$. It has the shape of a triangle with its base along the x axis: the electron returns practically along this axis.

Figure 8 suggests that the main contribution to the harmonic emission rate comes from travel times shorter than $0.5T$. In Fig. 12(a) we investigate in more detail trajectories that correspond to these travel times. The shortest orbit presented (bold solid line) has $\mathrm{Re}\,\tau=0.223T$ and $n=19$. The electron on this trajectory is never further away from the origin than 5 a.u. Strictly speaking, the picture of quantum orbits has little physical significance in this case, since the orbits never leave the region of a realistic binding potential. Emission of the associated harmonic is genuinely quantum mechanical and the visualization in terms of classical orbits does little to elucidate the physics. However, for increasing n (and, also, increasing Re τ) Fig. 12(a) shows the orbits becoming longer and longer. The orbit that corresponds to the maximal harmonic order $n=51$ has already been discussed above. Upon a further increase of Re τ, the electron's excursion becomes still larger, but the corresponding harmonic energy reduces (cf. the dotted curve labeled 43). This agrees with what is expected from the curve $n \equiv n(\mathrm{Re}\,\tau)$ plotted in the upper panel of Fig. 8.

The velocities (25) corresponding to the orbits of Fig. 11(a) are displayed in Fig. 11(b), and the electric-field vector $\mathbf{E}(t)$ of the driving field responsible for these harmonics is traced in Fig. 12(c) over its period from $-T/2$ to $T/2$. The initial (ionization) times and the final (recombination) times of the four harmonics considered in Fig. 12(a) are marked by stars and filled circles, respectively, and the numbers in Figs. 12(b,c) indicate the corresponding harmonic orders n. For example, the electron that recombines emitting the harmonic $n=51$ is ''born'' at $t=-0.1211T$ with a large velocity component in the negative y-axis direction. Under the action of the force $\mathbf{F}(t)=-e\mathbf{E}(t)$, both velocity components increase. The x component of the electric field changes its sign at the point $\mathbf{E}(0)=\mathbf{0}$, so that the electron's velocity component v_x starts decreasing. In contrast, the component v_y keeps increasing, up to the final time $t=t_f$, when both v_y and $|v_x|$ have maxima. A similar analysis can be done for the other values of n. For all cases presented in Fig. 12, ionization happens near a maximum of the electric-field amplitude $|\mathbf{E}(t)|$, so that the probability of the process is high. From Fig. 12(b) it follows that the kinetic energy $m\mathbf{v}^2(t_f)/2$ has a maximum for the curve labeled 51, which agrees with our previous results.

The orbits depicted in Fig. 12(a) (excluding the lowest harmonic number $n=19$) are quite similar to the orbits for HHG in a linearly polarized field. The reason becomes clear from Fig. 12(c). In between the start time and the return time the x component of the electric field changes from its negative maximum to (and beyond) its positive maximum while, in comparison, its y component remains small. Its effect is compensated by the y component of the initial velocity (otherwise, the electron would be unable to return to the origin). However, according to Fig. 12(b), this initial y component gradually increases from $n=19$ to $n=43$ (dotted curve), and in consequence, the intensities of the harmonics decrease. This pattern repeats itself three times during each cycle of the field, each time rotated by 120°. If one were able to separate the contribution to the harmonic spectrum from just one-third of the period, the polarization of the harmonics would be largely linear. It is the superposition of the three contributions from each cycle that generates the circular polarization of the harmonics.

VI. EXACT SADDLE-POINT ANALYSIS

In this section, we will consider the exact numerical solutions of the SPM equations (8)–(10) for the same example as in Sec. V A, not making the approximation of a real return time t_f. The easiest way to extract the physical information from these solutions is to present the imaginary part of the final (recombination) time t_f as a function of the real part of the travel time τ. This is done in Fig. 13(a), for the solutions such that Re τ does not exceed two optical cycles. For each value of the harmonic order n, which we continuously

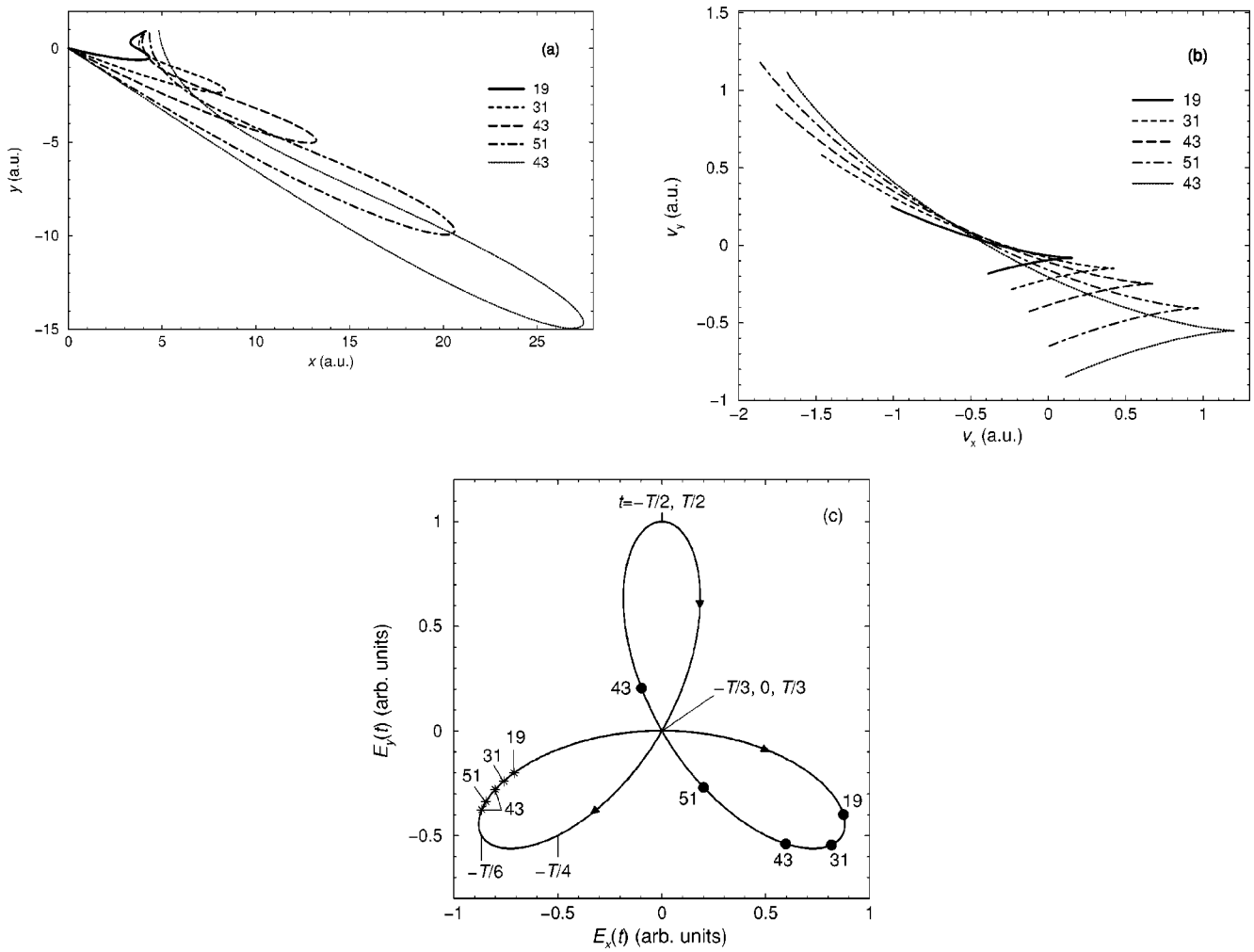

FIG. 12. Electron trajectories (a) and velocities (b) for some representative examples of short travel times $\mathrm{Re}\,\tau < T/2$. The laser field and atomic parameters are the same as in Figs. 8 and 11. The respective values of the harmonic order n are given to the right of the curves. (c) The curve traced out by the electric-field vector $\mathbf{E}(t)$ for $-T/2 \leqslant t \leqslant T/2$ in the direction specified by the arrows. For some points on the curve, the time t is indicated. The times for which the investigated orbits (a) and (b) start and terminate are marked by stars and filled dots, respectively, and the respective harmonic orders.

change from $n=4$ to $n=70$, we have found 11 solutions (t_i, t_f), denoted by the numbers in italics in Fig. 13(a). We restrict the plot of $\mathrm{Im}\,t_f/T$ to the narrow interval $-0.05 \leqslant \mathrm{Im}\,t_f/T \leqslant 0.05$ because for large values of $\mathrm{Im}\,t_f/T$ the probability of the HHG process is low. Practically, already for $|\mathrm{Im}\,t_f/T| \geqslant 0.01$ the harmonic emission rates are all but negligible.

Figure 13(a) must be compared with Fig. 8. It contains much the same, but also some additional information. First, we notice that for some particular values of $\mathrm{Re}\,\tau$ the quantity $\mathrm{Im}\,t_f/T$ goes to infinity. These values correspond exactly to the extrema of $n(\mathrm{Re}\,\tau)$ in the upper part of Fig. 8. We divide the curve $n(\mathrm{Re}\,\tau)$ into segments such that each segment is bordered by two adjacent extrema. Then each segment corresponds to a particular solution that is labeled by a number in italics in Fig. 13(a). We can see by inspection how the saddle-point method heals a deficiency of the semiclassical three-step model: the latter is unable to describe harmonics above or below the respective extrema in Fig. 8. In contrast, the saddle-point method reproduces those as well, since it keeps the imaginary part of the return time, which increases quickly when the harmonic number exceeds a classical cutoff (or goes below a minimum). This can be followed in Fig. 13(a) by means of the occasional values of the harmonic numbers that are provided. In general, the larger the absolute value of $\mathrm{Im}\,t_f$, the smaller is the contribution to the harmonic spectrum.

This comparison between the semiclassical three-step model and the exact saddle-point analysis is made quantitative in Fig. 13(b). In its upper part, we compare $n(\mathrm{Re}\,\tau)$ calculated from the exact saddle-point method (the broken curve) and from the semiclassical three-step model (the solid line, reproduced from Fig. 8). This shows that the two results are virtually identical except near the extrema of $n(\mathrm{Re}\,\tau)$ and for very short times $\mathrm{Re}\,\tau/T$. The exact saddle-point method being fully quantum mechanical does not yield extrema of the harmonic number. Also, for very short travel times, the former exhibits a gap in the travel times: the trajectories *2* and *1* maintain a finite distance with respect to the travel time $\mathrm{Re}\,\tau$. Their closest approach occurs precisely at the har-

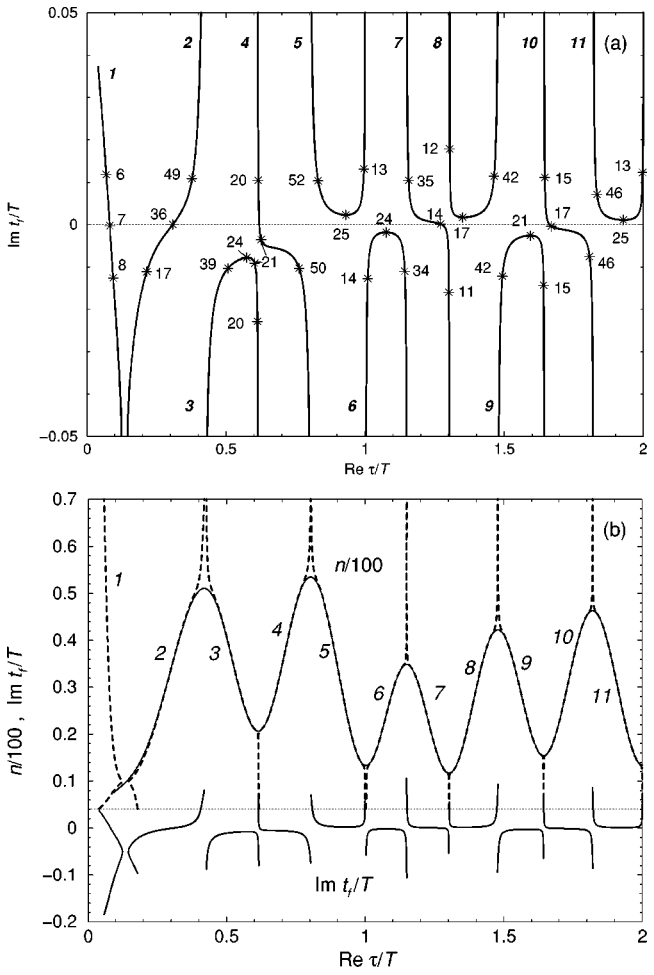

FIG. 13. (a) The imaginary part of the recombination time t_f as a function of the real part of the travel time τ, obtained from the exact solutions of the saddle-point equations (8)–(10). Notice that $\mathrm{Im}\, t_f$ is a single-valued function of $\mathrm{Re}\, \tau$ except for very short times, cf., part (b). In some representative cases marked by stars, the values of the harmonic order corresponding to a given $\mathrm{Re}\, \tau$ are indicated. (b) Upper part: Comparison of the exact saddle-point analysis (broken lines) to the semiclassical three-step model (solid lines, reproduced from Fig. 8). The harmonic numbers have been divided by 100 so that they fit on the same scale with $\mathrm{Im}\, t_f/T$, which is plotted in the lower part, reproduced from part (a), but on an expanded scale for the vertical axis. In (a) and (b), the laser field and the atomic parameters are the same as in Fig. 8. For the interval of $\mathrm{Re}\, \tau$ covered in the figure, we have found 11 solutions which are labeled by numbers in italics.

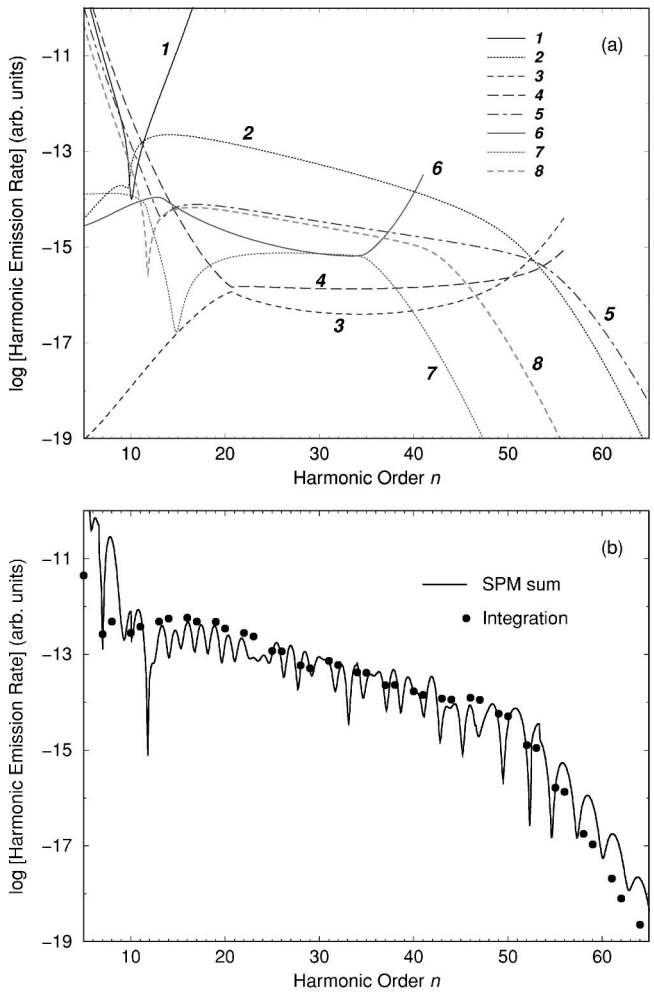

FIG. 14. Logarithm (base 10) of the harmonic emission rate in arbitrary units as a function of the harmonic order for the same laser field and atomic parameters as in Fig. 8. (a) Partial contributions of each of the first eight solutions of the SPM equations that are shown in Fig. 13. (b) Comparison of the saddle-point approximation (including the first 12 saddle-point solutions) (full line) and the exact SFA result obtained by numerical integration (filled circles).

monic corresponding to the binding energy of the model atom. In the lower part of Fig. 13(b), the curves $\mathrm{Im}\, t_f/T$ of Fig. 13(a) are redrawn on an expanded vertical scale. This allows one to scrutinize the behavior of $\mathrm{Im}\, t_f$ when the trajectories *2* and *1* approach each other.

We will now investigate some of the solutions in detail. The first solution *1* from Fig. 13 corresponds to small values of the travel time and, therefore, to electrons that have not spent enough time in the laser field to acquire significant kinetic energy from it. These electrons contribute only to very low values of n and are not relevant to the explanation of the plateaus and their cutoffs. In fact, the corresponding harmonics are below the continuum threshold and neither amenable to the semiclassical three-step model nor to the saddle-point method. Nevertheless, we have included them for completeness. The second solution (labeled *2*) is the most important one. This follows from the analysis of Sec. V [cf. Fig. 8 where it extends up to the first maximum of $n(\mathrm{Re}\, \tau)$], and we will confirm it below by the direct calculation of its contribution. This solution intersects the axis $\mathrm{Im}\, t_f = 0$. We have marked by stars three representative harmonic orders that about delineate the region of harmonics where the solution *2* makes significant contributions. Figure 8 suggests that the solutions *3*, *4*, and *9–11* in Fig. 13 are not important and this will be confirmed below. However, the solutions *5–8*, according to Fig. 8, make non-negligible contributions to the harmonic emission rate. The relevant values of n for each of these solutions are denoted in Fig. 13(a).

In Fig. 14(a) we present the partial harmonic emission rates, calculated using Eqs. (3) and (7), that correspond to the

first eight solutions from Fig. 13. The most important conclusion is that the solution *2* essentially dominates the entire spectrum up to the final cutoff. This is the solution with travel times around $T/3$ whose electronic orbits we have investigated closely in Fig. 12. Also, as suggested by Fig. 8, the solutions *3* and *4* make the smallest contribution. Near every maximum of the function $n(\mathrm{Re}\,\tau)$ in Fig. 8 two solutions contribute. This is reflected in Fig. 14 by the intersection of their contributions in the high-energy part of the spectrum. For example, partial rates of the solutions *2* and *3* intersect at the harmonic order 53, those of the solutions *4* and *5* at $n=54$, those of *6* and *7* at 34, and so on. The contribution of one of these pairs increases exponentially after such an intersection and must be discarded. If it were possible to give a rigorous mathematical justification of the steps leading from the T matrix (4) to its saddle-point approximation (7) then such a prescription would be part of it. Since such a rigorous derivation of the saddle-point evaluation of a five-dimensional integral appears to be out of the question, we have to accomplish this based on physical intuition. For example, the contributions of the solutions labeled *3*, *4*, and *6* out of the set discussed above have to be dropped after the points of intersection. This problem is also discussed in Ref. [20].

In a way, the analysis of the harmonic spectrum in terms of quantum trajectories leads to complementary conclusions for the two counter-rotating circular polarizations as compared to the standard situation of one linearly polarized monochromatic driving field. In the latter case, there are essentially two quantum trajectories which produce a pronounced interference pattern within the plateau. However, beyond the cutoff just one trajectory still contributes (the other one becomes unphysical and has to be dropped) and, consequently, the interferences cease, the spectrum decreases smoothly, and the phases of the harmonics lock [1,22]. On the other hand, in the case of the two bichromatic circular polarizations, just one trajectory (solution *2*) dominates the entire spectrum up to the cutoff. This one keeps contributing beyond the cutoff, but from there on it has to compete with another one (solution *5*). Hence, the plateau is comparatively smooth while the region beyond the cutoff exhibits a typical interference pattern, cf. Fig. 14(b) (in fact, this pattern only shows when the harmonic number is continuously varied).

Finally, in Fig. 14(b) we compare the results of a numerical calculation of the T matrix (4), obtained by the numerical integration and the fast Fourier transform of Eqs. (4)–(6) to its saddle-point evaluation (7) including the first 12 solutions of the saddle-point equations. The latter curve is labeled SPM. It was obtained considering the harmonic order n as a continuous parameter. The interferences between the contributions from different trajectories are better visible this way. Except for the lowest harmonics, the agreement between the exact numerical computation and the saddle-point approximation is quite good.

VII. CONCLUSIONS

In the context of an increasing interest for the generation of circularly polarized high-order harmonics, we presented an efficient method for their generation. We have reconsidered a method proposed previously for the generation of such harmonics, a driving field being the superposition of two circularly polarized fields with frequencies ω and 2ω that rotate in opposite directions within the same plane, and extended it to higher laser intensities. Our calculations show that the harmonic spectrum exhibits two plateaus: a shorter plateau with higher intensity is superposed on a longer one with lower intensity. We explained the features of these plateaus and their cutoffs in terms of the Lewenstein model, using an approximate semiclassical three-step model as well as the more complete saddle-point analysis in terms of complex electron trajectories. The semiclassical three-step model also starts from the saddle-point equations, but approximates the return time as a real quantity. This leads to significant simplifications and makes this model a useful tool for arbitrary configurations of the incident laser field. Using the intensity ratio of the two field components as a parameter, we optimized the harmonic spectrum with respect to the harmonic order (obtaining the cutoff law in the process), or with respect to the harmonic emission rate. We have also identified and discussed the electron trajectories that give the dominant contribution to the harmonic emission rate. We analyzed the influence of imperfect circular polarization of the high-frequency laser field component on the harmonic emission rates and found it to be small. It degrades, however, to some extent the circular polarization of the harmonics. The saturation intensity for the two-color circularly polarized field is unknown (cf. Ref. [23]). If it should exceed the saturation for a linearly polarized field by, say, just 50%, then this field produces harmonics more efficiently throughout most of the spectrum.

In this paper we have concentrated on harmonic emission by one single atom. For the practical relevance of the scheme that we investigated, the collective response of a gas sample is decisive. Because both circularly polarized components of our driving field propagate in the same direction, the conditions for phase matching are not very different [5] from harmonic generation in the standard situation of one linearly polarized driving field, cf., e.g., Ref. [1]. An adequate treatment of propagation must also include the effects of ionization of the atoms in the gas sample. Nothing is known about total ionization rates by the field that we considered. Owing to the genuine three dimensionality of all this, a reliable calculation of the collective response will not be easy.

We can summarize the reason for the surprising efficiency of harmonic generation by a single atom due to the two counter-rotating circularly polarized fields as follows. The strongest contribution to the harmonic emission rates comes from those orbits with rather short travel times such that $\mathrm{Re}\,\tau \approx T/3$. Some of them are depicted in Fig. 12(a), and they do not look very different from the one-dimensional orbits responsible for harmonic generation by a linearly polarized field. Indeed, the analysis of Fig. 12(c) shows that they are generated during those parts of the optical cycle where the field traces out a path that is (to lowest approximation) almost linear. Figure 1(a) shows that for all but extreme ratios of the intensities I_1 and I_2 one cycle of the field comprises

three such segments. However, for each such segment, the field also has a much smaller component that is perpendicular to the linear path. The impact of this component must be cancelled by an appropriate initial velocity. The larger this initial velocity component, the smaller is the contribution to harmonic emission. Inspection of Fig. 1(a) shows that the afore-mentioned counterproductive component of the electric-field vector has an average of about zero for the intensity distribution ''2+4,'' and we saw in Fig. 5 that it was this configuration that produced the most intense harmonics. Finally, it is the superposition of the contributions from the three segments of one optical cycle (rotated relative to each other by 120°) that produced the circular polarization of the emitted harmonics.

Figure 1(b) depicts the electric-field vector for the case of corotating polarizations. A quick glance makes clear that none of the above applies here anymore, and this provides an intuitive understanding of the virtual absence of high-harmonic generation in this case.

ACKNOWLEDGMENTS

D.B.M. gratefully acknowledges support from the Alexander von Humboldt Foundation. This work was supported in part by Deutsche Forschungsgemeinschaft.

[1] P. Salières, A. L'Huillier, Ph. Antoine, and M. Lewenstein, Adv. At., Mol., Opt. Phys. **41**, 83 (1999).
[2] H. Eichmann, A. Egbert, S. Nolte, C. Momma, B. Wellegehausen, W. Becker, S. Long, and J. K. McIver, Phys. Rev. A **51**, R3414 (1995).
[3] S. Long, W. Becker, and J. K. McIver, Phys. Rev. A **52**, 2262 (1995); A. Lohr, S. Long, W. Becker, and J. K. McIver, in *Super-Intense Laser-Atom Physics IV*, edited by H. G. Muller and M. V. Fedorov (Kluwer, Dordrecht, 1996), p. 477.
[4] X. M. Tong and S. I. Chu, Phys. Rev. A **58**, R2656 (1998).
[5] W. Becker, B. N. Chichkov, and B. Wellegehausen, Phys. Rev. A **60**, 1721 (1999).
[6] V. Averbukh, O. E. Alon, and N. Moiseyev, Phys. Rev. A **60**, 2585 (1999).
[7] B. Borca, A. V. Flegel, M. V. Frolov, N. L. Manakov, D. B. Milošević, and A. F. Starace (unpublished).
[8] J. L. Krause, K. J. Schafer, and K. C. Kulander, Phys. Rev. Lett. **68**, 3535 (1992); K. C. Kulander, K. J. Schafer, and J. L. Krause, in *Super-Intense Laser-Atom Physics*, Vol. 316 of *NATO Advanced Studies Institute, Series B: Physics*, edited by B. Piraux, A. L'Huillier, and K. Rzążewski (Plenum, New York, 1993), p. 95.
[9] P. B. Corkum, Phys. Rev. Lett. **71**, 1994 (1993).
[10] R. Kopold, D. B. Milošević, and W. Becker, Phys. Rev. Lett. (to be published).
[11] A. L'Huillier, M. Lewenstein, P. Salières, Ph. Balcou, M. Yu. Ivanov, J. Larsson, and C.-G. Wahlström, Phys. Rev. A **48**, R3433 (1993); M. Lewenstein, Ph. Balcou, M. Yu. Ivanov, A. L'Huillier, and P. B. Corkum, *ibid.* **49**, 2117 (1994).
[12] V. A. Pazdzersky and V. I. Usachenko, Laser Phys. **7**, 692 (1997).
[13] D. B. Milošević and F. Ehlotzky, Phys. Rev. A **58**, 2319 (1998).
[14] D. B. Milošević (unpublished).
[15] L. V. Keldysh, Zh. Éksp. Teor. Fiz. **47**, 1945 (1964) [Sov. Phys. JETP **20**, 1307 (1965)]: F. H. M. Faisal, J. Phys. B **6**, L89 (1973); H. R. Reiss, Phys. Rev. A **22**, 1786 (1980); **42**, 1476 (1990).
[16] D. B. Milošević and B. Piraux, Phys. Rev. A **54**, 1522 (1996).
[17] W. Becker, A. Lohr, M. Kleber, and M. Lewenstein, Phys. Rev. A **56**, 645 (1997).
[18] M. V. Ammosov, N. B. Delone, and V. P. Krainov, Zh. Éksp. Teor. Fiz. **91**, 2008 (1986) [Sov. Phys. JETP **64**, 1191 (1986)].
[19] N. L. Manakov, Zh. Éksp. Teor. Fiz. **110**, 1244 (1996) [Sov. Phys. JETP **83**, 685 (1996)].
[20] R. Kopold, W. Becker, and M. Kleber, Opt. Commun. (to be published).
[21] This is the case for linear polarization and for the fields considered in this paper, but not in general. For example, one may convince oneself that there are several curves $n=n(\mathrm{Re}\,\tau)$ for a linearly polarized two-color field; cf. C. Figueira de Morisson Faria, M. Dörr, W. Becker, and W. Sandner, Phys. Rev. A **60**, 1377 (1999).
[22] P. Salières, A. L'Huillier, and M. Lewenstein, Phys. Rev. Lett. **74**, 3776 (1995).
[23] L. F. DiMauro and P. Agostini, Adv. At., Mol., Opt. Phys. **35**, 79 (1995).